nature physics

Article

https://doi.org/10.1038/s41567-022-01874-8

Non-equilibrium spectral phase transitions in coupled nonlinear optical resonators

Received: 8 February 2022

Accepted: 9 November 2022

Published online: 19 January 2023

Check for updates

Arkadev Roy[1], Rajveer Nehra[1], Carsten Langrock[2], Martin Fejer[2] & Alireza Marandi[1]

Coupled systems with multiple interacting degrees of freedom provide a fertile ground for emergent dynamics, which is otherwise inaccessible in their solitary counterparts. Here we show that coupled nonlinear optical resonators can undergo self-organization in their spectrum leading to a first-order phase transition. We experimentally demonstrate such a spectral phase transition in time-multiplexed coupled optical parametric oscillators. We switch the nature of mutual coupling from dispersive to dissipative and access distinct spectral regimes of the parametric oscillator dimer. We observe abrupt spectral discontinuity at the first-order transition point. Furthermore, we show how non-equilibrium phase transitions can lead to enhanced sensing, where the applied perturbation is not resolvable by the underlying linear system. Our approach could be exploited for sensing applications that use nonlinear driven-dissipative systems, leading to performance enhancements without sacrificing sensitivity.

Coupled systems are omnipresent, ranging from neuronal connections in biological brains, artificial neural networks, social networks, power grids, circadian rhythms and reaction-diffusion chemical systems[1]. The nonlinear dynamics and the ensuing collective behaviours of coupled systems are remarkably richer than isolated individual systems[2–9]. These networks are endowed with complex physics that can have profound consequences on sensing[10] and computing[11,12].

Emergent phenomena in complex systems are ubiquitous and some paradigmatic examples of these non-equilibrium phenomena includes synchronization[13,14] and pattern formation[15–21]. Gain competition and/or energy exchange among the components of a many-body system on a microscopic scale can lead to emergent macroscopic behaviours[22] including the appearance of Turing patterns[23], coherent oscillation[24] and mode locking[25,26]. Understanding and engineering phase transitions in driven-dissipative systems constitutes a new frontier of many-body physics and non-equilibrium dynamics[27,28]. Non-equilibrium driven-dissipative systems open new possibilities and opportunities that are not present in their equilibrium counterparts. For instance, the time crystal is a non-equilibrium phase of matter that is believed to be realizable in out-of-equilibrium settings[29,30]. Photonics provides a congenial platform to engineer the drive and the dissipation for the exploration of non-equilibrium emergent phases and dynamical phase transitions[2,15,31–33].

A phase transition is associated with the qualitative change in the system behaviour as a control parameter is varied across a critical and/or transition point. An order parameter is often used to characterize systems exhibiting critical behaviours. A discontinuity in the order parameter and its derivative is a universal signature of first-order and second-order phase transitions, respectively[27]. Such abrupt discontinuities have been leveraged in transition-edge sensors to perform ultra-sensitive measurements down to single-photon levels[34]. Engineering such discontinuities in driven-dissipative systems is highly desirable for the development of high-sensitivity transition-edge sensors that are governed by non-equilibrium dynamics and are, therefore, not impaired by the slow dynamics that limit their counterparts based on thermodynamic equilibrium phase transitions[35]. A promising approach to quantum sensing involves the exploitation of quantum fluctuations in the vicinity of a critical point to improve the measurement precision. Theoretical studies indicate that sensors based on driven-dissipative phase transitions in parametric nonlinear resonators can be a useful resource in this regard[36].

Nonlinearity can potentially endow superior sensing capabilities that can attain performance enhancements of several orders

[1]Department of Electrical Engineering, California Institute of Technology, Pasadena, CA, USA. [2]Edward L. Ginzton Laboratory, Stanford University, Stanford, CA, USA. e-mail: marandi@caltech.edu

https://doi.org/10.1038/s41567-022-01874-8

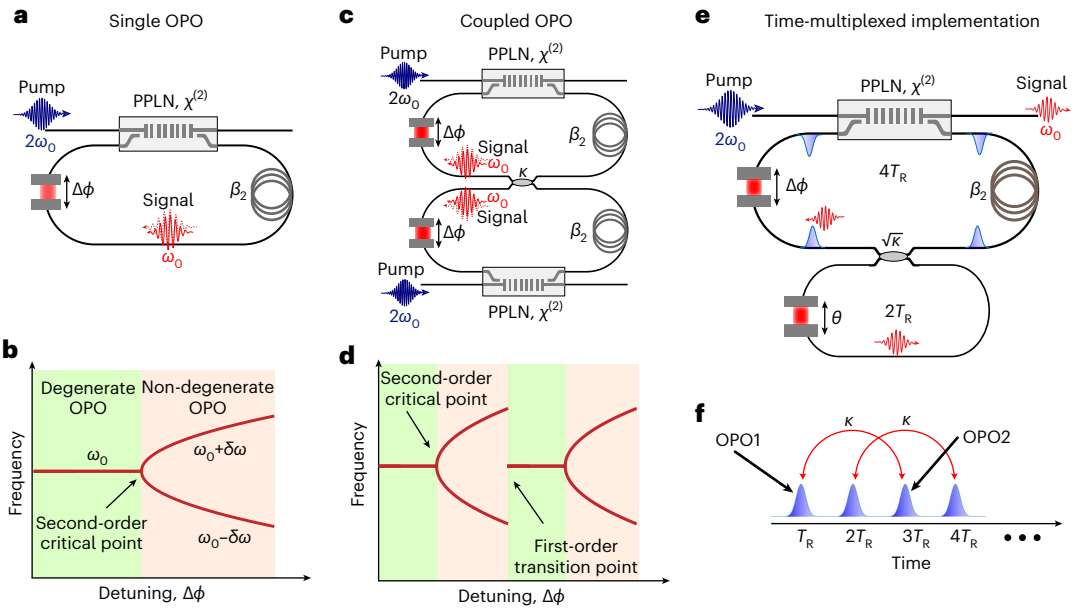

Fig. 1 | Non-equilibrium phase transitions in single and coupled OPOs. **a**, Schematic of a single OPO showing the non-resonant pump ($2\omega_0$) and the resonant signal and/or idler (ω_0) interacting via phase-matched quadratic ($\chi^{(2)}$) nonlinearity alongside the detuning ($\Delta\phi$) element and the intracavity dispersion β_2. **b**, Existence of a second-order spectral phase transition in a single OPO where, at the critical detuning, the OPO transits between the degenerate and the non-degenerate oscillation regimes. **c**, Schematic of a coupled OPO system with the mutual coupling κ. **d**, Existence of a first-order spectral phase transition in coupled OPOs featuring an abrupt spectral discontinuity at the first-order transition point. **e**, Time-multiplexed implementation of the coupled OPOs consisting of a main OPO cavity (with a round-trip time of $4T_R$) that is twice as long as the linear coupling cavity. The cavity detuning is controlled using a detuning element ($\Delta\phi$) in the main cavity, while the detuning element in the coupling cavity affects the coupling phase θ. **f**, Illustration of the pulses circulating in the time-multiplexed implementation, where the pulse-to-pulse separation is given by the repetition period of the driving pump laser and the coupling exists between alternate pulses, thereby constituting a coupled OPO system.

of magnitude over those that rely on linear dynamics alone[37–39]. For instance, nonlinearity-induced non-reciprocity can amplify the Sagnac effect in the vicinity of a symmetry-breaking instability[39]. Similarly, it has been proposed that operating close to the region of bistability can lead to strong enhancement to refractive-index sensitivity[40]. However, experimental demonstrations of the aforementioned nonlinear advantage remain scarce.

In this work, we exploit the rich dynamics of coupled optical parametric oscillators (OPOs) to realize non-equilibrium phase transitions. We demonstrate first-order spectral phase transitions, and observe abrupt discontinuity at the transition point corresponding to the system's sudden self-organization between degenerate and non-degenerate oscillation regimes. We show that the system of coupled OPOs exhibits a qualitatively different behaviour with the alteration of their mutual coupling from dispersive to dissipative. We also present nonlinearly enhanced sensing in the driven-dissipative system under consideration, where the applied perturbation remains unresolved by the underlying linear system. Our results on non-equilibrium behaviour in a system of coupled nonlinear resonators can have far-reaching consequences in the domains of sensing and computing.

Results

The building block of our coupled system is a doubly resonant OPO that is parametrically driven by a pulsed pump centred around $2\omega_0$, where ω_0 is the frequency at degeneracy corresponding to the half-harmonic (Fig. 1a)[41]. The cavity hosts multiple longitudinal frequency modes around the half-harmonic frequency, where the signal and/or idler resides. The distribution of these frequency modes is determined by the cavity group velocity dispersion (GVD, β_2), while the interaction between them is facilitated by the quadratic nonlinearity ($\chi^{(2)}$). The energy exchange between the pump and the signal ($\omega_0 + \delta\omega$) and the idler ($\omega_0 - \delta\omega$) modes is governed by the energy and momentum conservation relations. The OPO exists in a trivial state (zero mean field) below the threshold, which loses stability leading to parametric oscillation as the gain is increased above the oscillation threshold. The oscillation proceeds via the modulational instability, and the OPO assumes a temporal frequency (fast-time-scale dynamics) ($\Omega = \delta\omega$, centred around the half-harmonic), corresponding to the maximum growth-rate of perturbations (Supplementary Section 9). Here $\delta\omega = 0$ corresponds to the degenerate oscillation, while $\delta\omega \neq 0$ corresponds to the non-degenerate oscillation regime. The temporal mode with the zero effective detuning experiences the maximum parametric gain. This can happen even in the presence of non-zero cavity detuning, where the GVD-induced detuning counterbalances the linear cavity detuning $\Delta\phi$. This mutual interplay of cavity detuning and GVD leads to a second-order spectral phase transition as shown in Fig. 1b (ref. 15). The critical detuning ($\Delta\phi = 0$) marks a soft transition between the degenerate and the non-degenerate parametric oscillation regimes.

However, this rich spectral behaviour observed in a single OPO does not extend linearly with the increase in system size, that is, to a network of coupled OPOs (Fig. 1c). It is well known that, in the realm of parity–time symmetric non-Hermitian systems, increasing the system size increases the order of the exceptional point[42]. Strikingly, we show that it is possible to realize a hard-transition (first-order transition) in a system of coupled OPOs, where a single OPO is only capable of featuring a soft transition (second-order transition). Our system of coupled OPOs represents a complex system enabling a rich interplay of nonlinearity, linear coupling (κ), multimode dynamics, dispersion, drive and dissipation. This can lead to an abrupt spectral discontinuity between the degenerate and non-degenerate oscillation regimes (Fig. 1d). We note that the phase transition considered here is of non-equilibrium nature, which is distinct from the typical thermodynamic transitions (see Supplementary Section 15 for further discussions).

https://doi.org/10.1038/s41567-022-01874-8

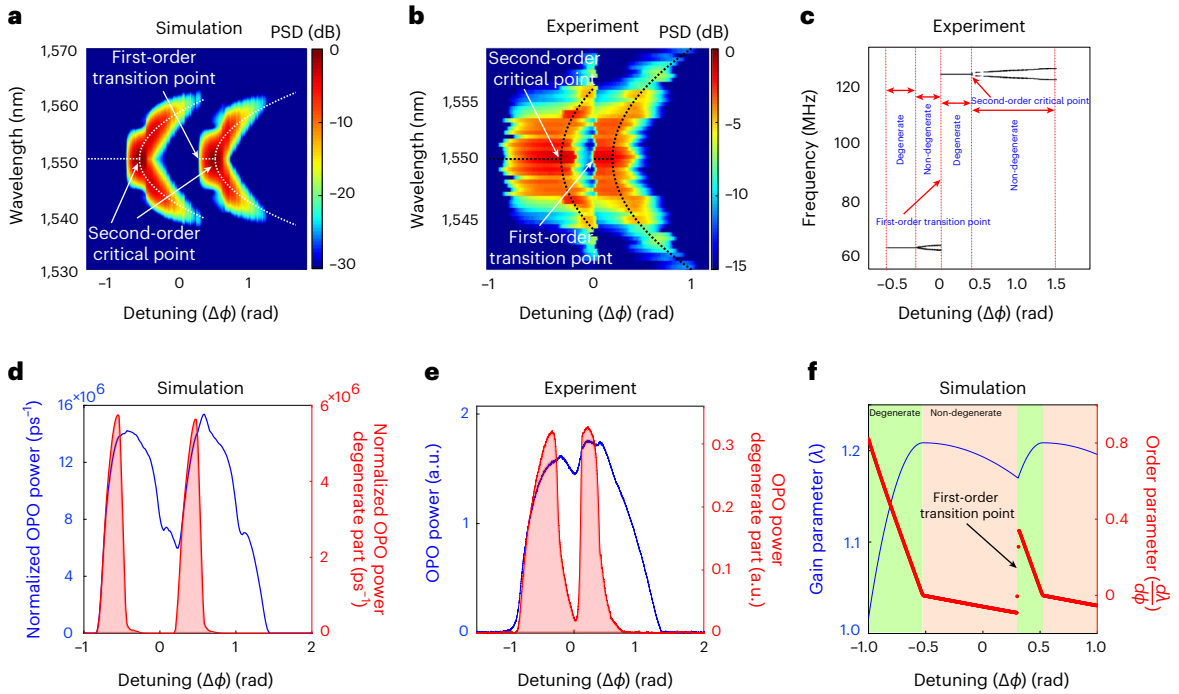

Fig. 2 | First-order spectral phase transition in coupled OPOs. a, Numerical simulation of the optical spectrum (power spectral density (PSD)) of coupled OPOs as a function of cavity detuning featuring the second-order phase transitions at the mode-splitting locations and the first-order phase transition. **b**, Experimentally obtained optical spectrum as a function of cavity detuning highlighting the abrupt spectral discontinuity at the first-order transition point. The idler part of the spectrum is constructed by mirror reflection about the half-harmonic line. **c**, RF beat-note spectrum indicating the distinct degenerate and non-degenerate oscillation regimes demarcated by the second-order critical points and the first-order transition point. **d**, Numerical simulation of the OPO power as a function of the detuning. The power contained in the degenerate part of the spectrum (1 nm of bandwidth around the half-harmonic frequency ω_o) is also plotted alongside showing two distinct degenerate oscillation regimes flanked by non-degenerate oscillation regimes. **e**, Coupled OPO power as a function of detuning obtained experimentally. The power contained in the degenerate regime has been extracted using a bandpass filter centred around the half-harmonic frequency. **f**, The order parameter (the derivative of the gain function) shows a discontinuity at the transition point, suggesting the existence of a first-order phase transition.

We implement coupled OPOs using time multiplexing[11,12,43] (Fig. 1e). This represents a synthetic dimension implementation, where the discrete time dimension provided by the equidistant pulses of a mode-locked laser has been utilized to realize a coupled OPO system without increasing the spatial complexity of realizing OPOs in two different cavities. In this two-cavity configuration the main cavity is twice as long as the coupling cavity. Specifically in our experiments, we chose the main cavity round-trip time to be four times the repetition period of the mode-locked laser (T_R). This ensures that the coupling cavity executes coupling between alternate pulses. Thus pulses occurring at time instants given by $(4n+1)T_R$ and $(4n+3)T_R$ or $(4n)T_R$ and $(4n+2)T_R$ (where n is an integer) constitute two sets of coupled OPOs (Fig. 1f) (Supplementary Section 12). Moreover, our time-multiplexed implementation allows us to mimic different types of coupling (dispersive, dissipative or hybrid)[44], because the phase of the coupling path can be altered by modifying the detuning of the coupling cavity. The detuning elements in the main cavity and the coupling cavity control the cavity detuning parameter ($\Delta\phi$) and the coupling phase θ independently.

The first-order phase transition in coupled OPOs emerges from the interplay of the supermodes of the coupled cavities and parametric gain. The dispersive coupling κ leads to mode hybridization between the modes of the coupled cavities. These supermodes can be either symmetric when the resonant fields are in phase or antisymmetric when they are out-of-phase. The frequency separation between them depends on the coupling strength κ. At a given excitation frequency, there exists a range of cavity detunings, where one of the supermodes is close to resonance while the other one is off-resonant. In those circumstances, we can consider the dominant supermode only, and the dynamics of the coupled system resembles a single OPO, albeit now in the supermode basis. This results in second-order phase transitions around the mode-splitting points as shown in Fig. 2a. However, in the range of cavity detunings in which the contribution from the supermodes are comparable, there occurs a competition between the two second-order spectral phase transitions (one centred around the symmetric supermode and the other centred around the asymmetric supermode). This gain competition enforces a spectral self-organization of the coupled OPOs leading to a sharp transition between non-degenerate and degenerate oscillation regimes as shown in Fig. 2a. This proceeds via a first-order phase transition, when the gain of the non-degenerate branch of the symmetric supermode ceases to be greater than the gain experienced by the degenerate branch of the asymmetric supermode (Supplementary Sections 2 and 3). The experimental results (Fig. 2b) of the optical spectrum corroborate the theory and the numerical simulations (the coupling factor realized experimentally is lower than the value assumed in the simulation).

The non-equilibrium phase transitions in coupled OPOs are further characterized by the radio-frequency (RF) measurements (Fig. 2c). A sync-pumped doubly resonant OPO in the non-degenerate regime generates a signal and an idler frequency comb with two carrier-envelope offset frequencies, which can be measured through beating with a local oscillator. The abrupt spectral discontinuity of this beat-note measurement unequivocally confirms the occurrence of the first-order phase transition. For non-degenerate (near-degenerate) doubly resonant OPO, the f_{CEO} can be deterministically estimated based on the OPO cavity detuning[45]. The doubly resonance condition is satisfied simultaneously for the signal and the idler to achieve the maximum

https://doi.org/10.1038/s41567-022-01874-8

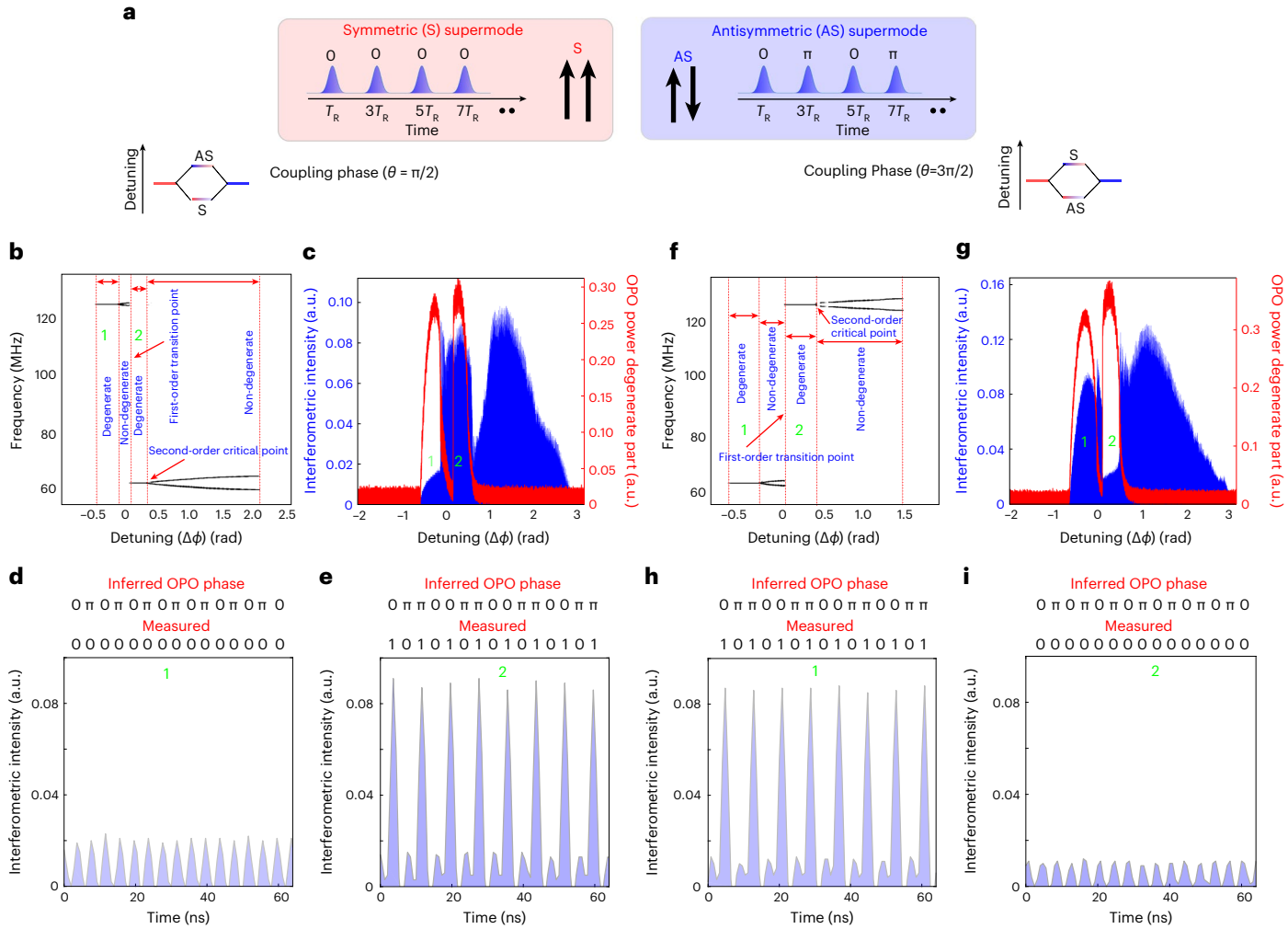

Fig. 3 | Supermodes of the coupled OPOs. a, Illustration of the supermodes and their associated manifestation in the time-multiplexed implementation. **b**, RF beat-note spectrum as a function of detuning in the presence of dispersive coupling with coupling phase $\theta = \pi/2$. **c**, The corresponding pulse pattern at the output of a single-pulse delayed Mach–Zehnder interferometer. The OPO power in the degenerate band is also plotted. **d**, The interferometric pulse pattern in the degenerate regime (marked as 1) shows that the OPO pulses are in phase, representing the symmetric supermode. **e**, The pulse pattern in the degenerate regime (marked as 2) shows that the OPO pulses are out of phase, representing the antisymmetric supermode. **f**,**g**, Similarly, the case with the dispersive coupling and coupling phase $\theta = 3\pi/2$ is considered, where the RF spectrum and the interferometer pulse pattern are displayed in **f** and **g**, respectively. **h**,**i**, The degenerate regime (marked as 1) shows that the OPO pulses constituting the coupled OPO are out of phase, implying the antisymmetric supermode (**h**), while the degenerate regime (marked as 2) shows that the OPO pulses are in phase indicating the symmetric supermode (**i**).

parametric gain. This fixes the carrier phase velocity, leaving the f_{CEO} to be determined by the effective group velocity of the signal and idler envelopes. The effective group velocity comprises the linear component that arises due to the material dispersion, and the contribution due to the nonlinear acceleration of the pulses arising because of the cavity nonlinear dynamics. The constraint to satisfy $f_{CEO,p} = f_{CEO,s} + f_{CEO,i}$ (where the subscripts p, s, and i denote pump, signal, and idler, respectively) along with the fixed frequency splitting relationship (the maximum gain principle described above) fixes the respective f_{CEO} of the signal and idler pulses uniquely to the cavity detuning. The output power of the coupled OPOs as a function of detuning is representative of the parametric gain, and leads to maximum conversion efficiencies at the second-order critical points at which the supermodes are resonant. This can be seen from the simulation and experimental results in Fig. 2d,e. The power contained in the spectrum centred around degeneracy is indicative of the degenerate regime of operation. The OPO output after passing through a bandpass filter centred around the half-harmonic frequency is also shown in Fig. 2d,e, which indicates the presence of two distinct degenerate regimes of operation separated by the non-degenerate oscillation regime. The order parameter (defined as the derivative of the gain parameter with respect to the detuning) exhibits a behaviour typical of a first-order phase transition with the characteristic discontinuity at the first-order transition point (Fig. 2f). The gain parameter (λ) reveals the underlying gain competition between the two supermodes.

The eigenvector composition of the supermodes can be unveiled from the pulse-pattern measurements in the time domain as illustrated in Fig. 3a. When the coupling phase (θ) equals π/2, the antisymmetric eigenmode has a higher frequency (corresponding to larger detuning) than its symmetric counterpart (Supplementary Section 2). The symmetric and the antisymmetric supermodes have distinct carrier-envelope offset frequencies as is evident from the RF spectrum (Fig. 3b). The pulse pattern is measured using a one-pulse delayed Mach–Zehnder interferometer (Fig. 3c) to infer the phases of the OPO pulses constituting the coupled OPOs. The coupled OPOs in the symmetric supermode-dominated degenerate regime (1) features OPO pulses that are in phase (Fig. 3d). In the antisymmetric supermode degenerate regime (2), the OPO pulses comprising the

https://doi.org/10.1038/s41567-022-01874-8

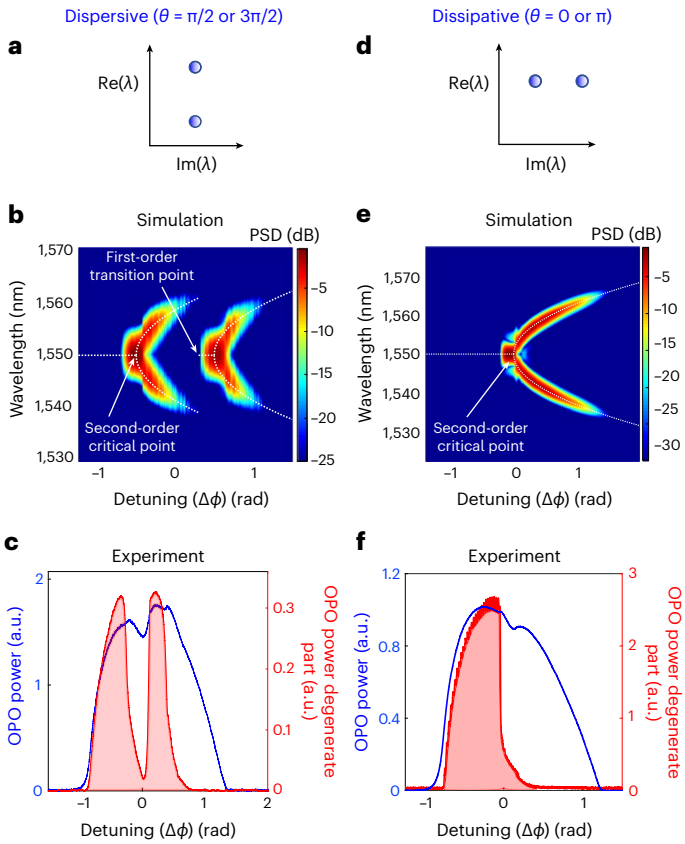

Fig. 4 | Dispersive versus dissipative coupling. a, Dispersive coupling between coupled resonators results in the splitting of the real part of the eigenvalue (spectrum), where both the supermodes experience identical dissipation. **b**, The existence of the mode hybridization in the real part of the spectrum enables the observation of two second-order spectral phase transitions centred around the mode splitting and the associated first-order transition point. **c**, OPO power as a function of detuning along with the power contained in the degenerate regime corroborates the existence of the underlying mode splitting. **d**, In the presence of dissipative coupling the supermodes experience different dissipation while their real part remains identical. **e**, The absence of mode hybridization in the real part of the spectrum precludes the observation of the first-order phase transition and only leads to features representative of the spectral behaviour of a single OPO. **f**, OPO power as a function of detuning showing the existence of a single degenerate regime confirming the absence of mode splitting with dissipative coupling.

coupled OPOs are out of phase (Fig. 3e). When the coupling phase is 3π/2, the frequency spectrum of the supermodes is reversed, with the symmetric supermode now associated with larger detuning. This is revealed in the corresponding measurements shown in Fig. 3f–i. This agrees with the results obtained from numerical simulations (Supplementary Section 2).

The spectral behaviour of the coupled OPOs drastically differs with the alteration of the nature of mutual coupling (κ). Modification of the coupling phase (θ) enables us to mimic dispersive (π/2 or 3π/2), dissipative (0 or π) or hybrid (intermediate phases) coupling schemes (Supplementary Sections 4 and 12). Dispersive coupling results in splitting in the real part of the eigenvalues (that is, mode splitting) where the supermodes experience an identical rate of dissipation (the imaginary part of the eigenvalue is the same) (Fig. 4a). This leads to spectral and temporal features resembling the aforementioned discussions (Fig. 4b,c). In stark contrast, dissipative coupling leads to splitting in the imaginary part of the eigenvalue where the supermodes experience disparate dissipation[44] (Fig. 4d). This property of the dissipative coupling is at the heart of the operation of optical coherent Ising machines[12] and recent demonstrations of topological dissipation[43]. Consequently, the absence of mode splitting is also reflected in the spectral (Fig. 4e) and the power (Fig. 4f) characteristics of dissipatively coupled OPOs. Dissipative coupling precludes the occurrence of a first-order spectral phase transition and shows the mere presence of a second-order phase transition.

The presence of non-equilibrium phase transitions with characteristic discontinuities opens up new opportunities in the domain of sensing. High-quality (Q)-factor optical resonators have been utilized for highly sensitive refractive-index perturbation measurements[46]. However, the requirement of a high quality factor for enhanced sensitivity results in an unavoidable trade-off with the bandwidth and hence limits the sensing speed. The non-equilibrium phase transition in coupled OPOs can circumvent this trade-off. Figure 5a shows the transmission of coupled optical resonators with different round-trip losses. The mode splitting is observed in the regime of high-Q (lower round-trip loss), while low-Q (high-bandwidth) resonators cannot resolve the mode-splitting structure. Remarkably, this mode splitting can be revealed even in the low-Q regime in the nonlinear case, where the coupled resonators are parametrically driven as coupled OPOs (Fig. 5b). The sensing parameter can be the phase detuning in the coupling cavity of the time-multiplexed architecture leading to a perturbation ($\delta\theta$) in the coupling phase (θ). In the presence of this coupling-phase perturbation, coupled high-Q linear resonators will respond with asymmetric mode splitting, where the degree of the asymmetry depends on the strength of the perturbation (Fig. 5c). The asymmetry also reflects the sign of the phase perturbation, which is an added advantage over high-Q linear cavity-based simple sensing arrangements, where the sensors can suffer from directional ambiguity[47]. This asymmetric mode-splitting behaviour cannot be resolved by low-Q coupled linear resonators. However, low-Q coupled OPOs can extract these features, which is shown in Fig. 5d,e by displaying the power contained in the degenerate part (using a bandpass filter). Results obtained from our low-Q (high gain and bandwidth) experimental setup agrees well with the simulations (Supplementary Section 1).

We quantify the sensitivity of the system using a normalized sensitivity metric and benchmark its performance in comparison with linear high-Q resonator-based sensors. Our sensing protocol is described in Fig. 6a, which constitutes a photodetector that registers the bandpass-filtered (centred around degeneracy) output signal. The system should be biased near the spectral phase transition critical points to exploit the maximum sensitivity, which can be ensured by active locking means[48]. The change of detected power y in the response of a detuning ($\Delta\phi$) perturbation ϵ can be drastically enhanced in the vicinity of the spectral phase transition point owing to the transition from degeneracy to the non-degenerate regime, which lies outside the spectral acceptance bandwidth of the bandpass filter. Our simplified sensing scheme is compatible with high-bandwidth measurements and does not involve the complex process of laser frequency scanning and/or sweeping. The normalized sensitivity is defined as: $S = \frac{1}{y_{\max}} \frac{\mathrm{d}y}{\mathrm{d}\Delta\phi}$. The sensitivity at the first-order transition point (Fig. 6c) is much higher as compared to its second-order counterpart (Fig. 6b)[35]. The enhanced sensitivity near the first-order transition point comes at a cost of drastically reduced dynamic range as compared to that based on the second-order critical point. Our simulation agrees with the data obtained experimentally (Fig. 6d). We provide further details on the experimental approaches to access such sensitivities in the Supplementary Information (Supplementary Section 17). The observed sensitivity enhancement is equivalent to a critically coupled linear high-Q cavity-based sensor with a Finesse of approximately 250 (a quality factor of 1 million at 1,550 nm with a cavity of 50 GHz free spectral range). This represents a dramatic enhancement of more than three orders of magnitude in terms of the sensitivity compared to the cold-cavity system, which had a Finesse of ~0.5. The sensitivity for a linear high-Q

https://doi.org/10.1038/s41567-022-01874-8

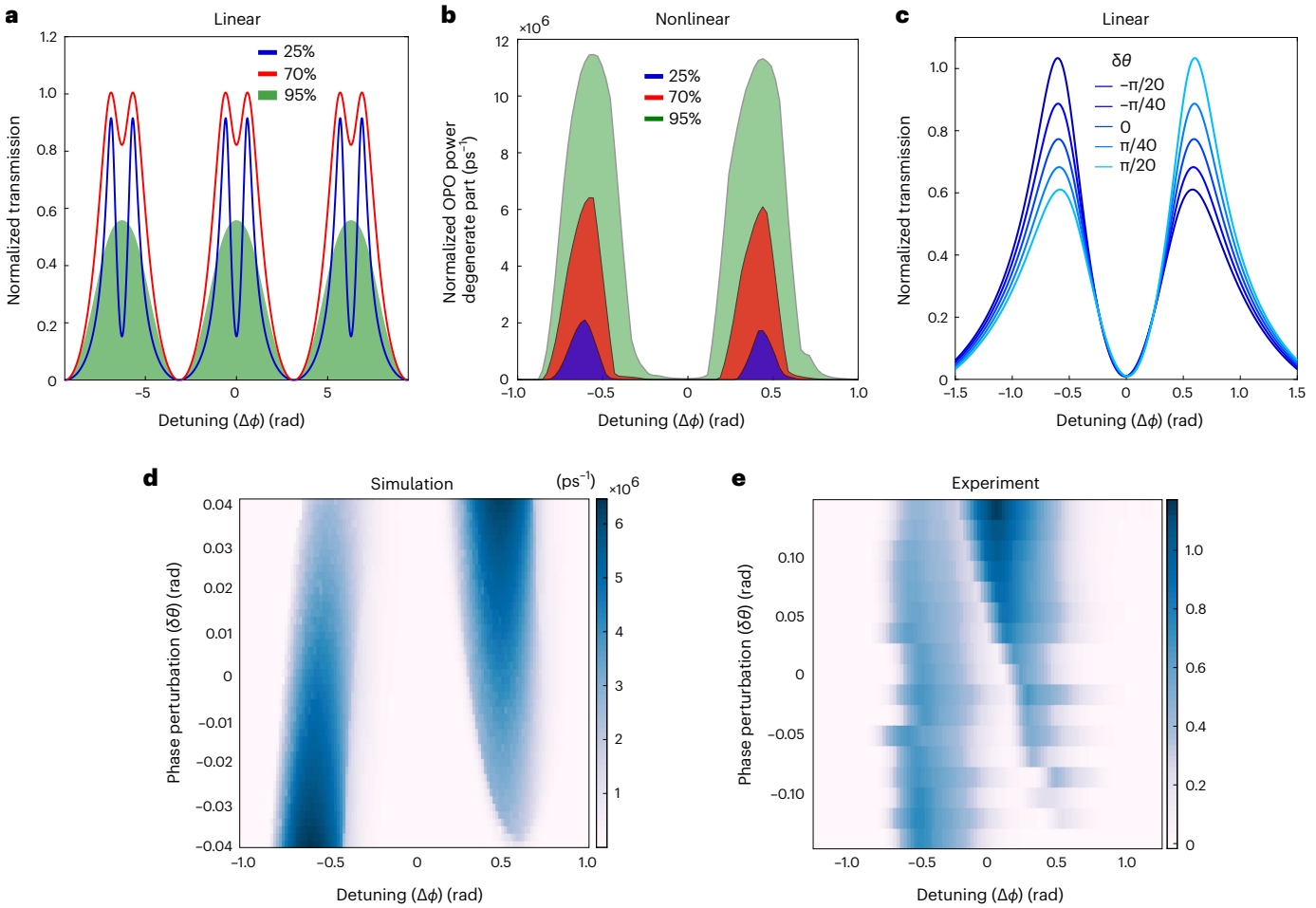

Fig. 5 | Enhanced sensing using non-equilibrium phase transitions. **a**, Transmission through coupled linear resonators with varying round-trip loss. With lower loss values (high-Q) the mode splitting is conspicuous, which disappears in the low-Q regime. **b**, Power contained in the degenerate regime of the coupled OPO as a function of detuning for various values of round-trip loss. In contrast to the linear case, this nonlinear regime could resolve the mode splitting even in the low-Q regime. **c**, Transmission in coupled linear resonators (high-Q regime) in the presence of applied perturbation expressed as the perturbation in the coupling phase ($\delta\theta$). The perturbation renders the coupling to be a hybrid of dispersive and dissipative, leading to asymmetric mode splitting. **d**,**e**, Power contained in the degenerate regime of the coupled OPO with varying perturbation in the low-Q regime obtained through numerical simulation (**d**) and experiments (**e**). Despite operating in the low-Q regime, the nonlinear dynamics could resolve the underlying asymmetric mode splitting in response to small coupling-phase perturbations.

based sensor is shown in Fig. 6e as a reference. With a combination of proper dispersion engineering and system design it is possible to exhibit sensitivity that is equivalent to a linear high-Q-based system with a Finesse exceeding 10^4. This is extremely important in circumventing the difficulties associated with achieving high-quality-factor cavities in an integrated platform when interfacing with sensing technologies[49]. Our work highlights the possibility of achieving sensitivity levels that are on a par with state-of-the-art sensing systems using easily accessible low-Q-based systems. The other alternative in terms of sensing scheme is to resort to RF domain measurements (Fig. 2c), where the signal-to-noise ratio can be improved by performing coherent averaging at the cost of reduced sensing bandwidth. These results indicate the potential of non-equilibrium spectral phase transitions for enhanced sensing (Supplementary Section 14).

Discussion

In summary, we have demonstrated the occurrence of first-order non-equilibrium phase transitions in coupled OPOs. We have experimentally characterized the spectral and the temporal features associated with this phase transition, and also revealed the eigenvector composition of the supermodes. We have highlighted the distinct spectral behaviours of coupled OPOs in the presence of dispersive and dissipative couplings. Finally, we have demonstrated the potential of these phase transitions in coupled OPOs for enhanced sensing. The results presented here can be directly relevant to other systems, including Faraday waves in hydrodynamics and parametrically forced mechanical or chemical systems. With the recent progress in the nanophotonic lithium niobate platform[50–52], exploration of extended lattices can become feasible, paving the way towards the study of emergent nonlinear phenomena in soliton networks and higher-dimensional lattices (Supplementary Section 8)[53]. The demonstrated phase transition can be modelled using the universal coupled Swift–Hohenberg equation and can be implemented also in Kerr nonlinear resonators[54,55]. The abrupt discontinuity at the first-order transition point and the associated spectral bistability can open new possibilities in the domain of precision sensing (Supplementary Section 6). The semiclassical regime considered in this work can be probed below the oscillation threshold[56], where a quantum image of the above-threshold spectral phase transition exists, which may lead to the co-existence of a quantum phase transition (Supplementary Section 7)[57]. Our study mainly focuses on the adiabatic regime, where the control parameter is varied gradually. Introduction of non-adiabaticity can lead to the Floquet dynamics

https://doi.org/10.1038/s41567-022-01874-8

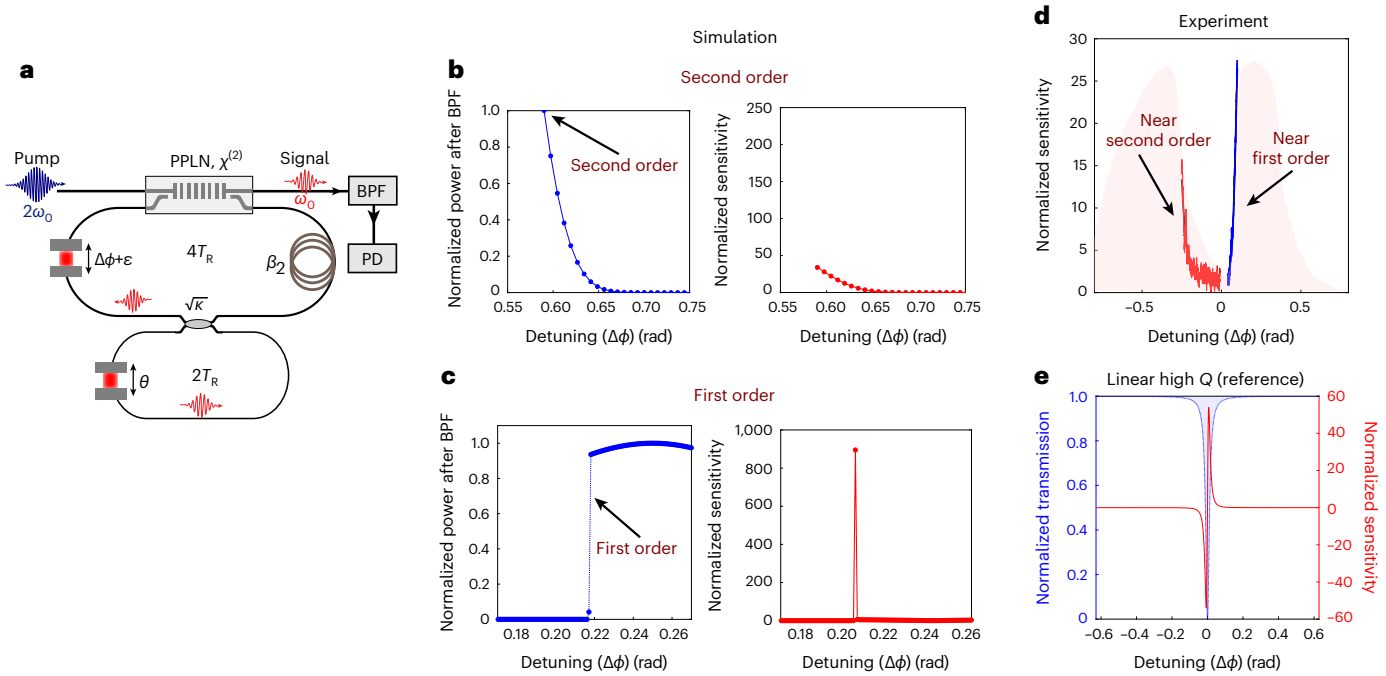

Fig. 6 | Sensitivity near the spectral phase transition points. a, Schematic depicting the sensing protocol involving the detection of the coupled OPOs output on a photodetector (PD) after passing through a bandpass filter (BPF) centred around degeneracy. **b**, Detected power (y) as a function of detuning ($\Delta\phi$) perturbation from the second-order critical point. The normalized sensitivity (S) is also shown, as obtained from numerical simulation. **c**, Same as in **b**, but for perturbations around the first-order transition point, showing enhanced sensitivity compared to its second-order counterpart. **d**, Normalized sensitivity obtained experimentally for operation near both the second-order critical point and the first-order transition point. This does not include the sharp discontinuity at the first-order transition point. **e**, The sensitivity that can be obtained from a critically coupled linear high-Q cavity-based sensor is shown for reference. The bandpass filter bandwidth is assumed to be 1 nm.

with enriched phase diagrams (Supplementary Section 13)[58]. Intriguing dynamics is also expected in the case of nonlinearly coupled resonators[59]. Analysis of noise mechanisms that could possibly constrain the achievable precision will be the subject of future studies. Our work lays the foundation for the exploration of emergent dynamics and critical phenomenon beyond the single-particle description and insinuates potential advances in sensing and computing.

Online content

Any methods, additional references, Nature Portfolio reporting summaries, source data, extended data, supplementary information, acknowledgements, peer review information; details of author contributions and competing interests; and statements of data and code availability are available at https://doi.org/10.1038/s41567-022-01874-8.

References

1. Watts, D. J. & Strogatz, S. H. Collective dynamics of 'small-world'networks. *Nature* **393**, 440–442 (1998).
2. Tikan, A. et al. Emergent nonlinear phenomena in a driven dissipative photonic dimer. *Nat. Phys.* **17**, 604–610 (2021).
3. Grigoriev, V. & Biancalana, F. Resonant self-pulsations in coupled nonlinear microcavities. *Phys. Rev. A* **83**, 043816 (2011).
4. Zhang, M. et al. Electronically programmable photonic molecule. *Nat. Photonics* **13**, 36–40 (2019).
5. Zhang, Y. et al. Squeezed light from a nanophotonic molecule. *Nat. Commun.* **12**, 2233 (2021).
6. Miller, S. A. et al. Tunable frequency combs based on dual microring resonators. *Opt. Express* **23**, 21527–21540 (2015).
7. Xue, X., Zheng, X. & Zhou, B. Super-efficient temporal solitons in mutually coupled optical cavities. *Nat. Photonics* **13**, 616–622 (2019).
8. Roy, A. et al. Nondissipative non-Hermitian dynamics and exceptional points in coupled optical parametric oscillators. *Optica* **8**, 415–421 (2021).
9. Okawachi, Y. et al. Demonstration of chip-based coupled degenerate optical parametric oscillators for realizing a nanophotonic spin-glass. *Nat. Commun.* **11**, 4119 (2020).
10. Guo, X. et al. Distributed quantum sensing in a continuous-variable entangled network. *Nat. Phys.* **16**, 281–284 (2020).
11. McMahon, P. L. et al. A fully programmable 100-spin coherent Ising machine with all-to-all connections. *Science* **354**, 614–617 (2016).
12. Marandi, A., Wang, Z., Takata, K., Byer, R. L. & Yamamoto, Y. Network of time-multiplexed optical parametric oscillators as a coherent ising machine. *Nat. Photonics* **8**, 937–942 (2014).
13. Jang, J. K. et al. Synchronization of coupled optical microresonators. *Nat. Photonics* **12**, 688–693 (2018).
14. Fruchart, M., Hanai, R., Littlewood, P. B. & Vitelli, V. Non-reciprocal phase transitions. *Nature* **592**, 363–369 (2021).
15. Roy, A., Jahani, S., Langrock, C., Fejer, M. & Marandi, A. Spectral phase transitions in optical parametric oscillators. *Nat. Commun.* **12**, 835 (2021).
16. Haken, H. Cooperative phenomena in systems far from thermal equilibrium and in nonphysical systems. *Rev. Mod. Phys.* **47**, 67 (1975).
17. Vaupel, M., Maitre, A. & Fabre, C. Observation of pattern formation in optical parametric oscillators. *Phys. Rev. Lett.* **83**, 5278 (1999).
18. Cross, M. C. & Hohenberg, P. C. Pattern formation outside of equilibrium. *Rev. Mod. Phys.* **65**, 851 (1993).
19. Ropp, C., Bachelard, N., Barth, D., Wang, Y. & Zhang, X. Dissipative self-organization in optical space. *Nat. Photonics* **12**, 739–743 (2018).

20. Taranenko, V. B., Staliunas, K. & Weiss, C. O. Pattern formation and localized structures in degenerate optical parametric mixing. *Phys. Rev. Lett.* **81**, 2236 (1998).
21. Oppo, G.-L., Yao, A. M. & Cuozzo, D. Self-organization, pattern formation, cavity solitons, and rogue waves in singly resonant optical parametric oscillators. *Phys. Rev. A* **88**, 043813 (2013).
22. Wu, F. O., Hassan, A. U. & Christodoulides, D. N. Thermodynamic theory of highly multimoded nonlinear optical systems. *Nat. Photonics* **13**, 776–782 (2019).
23. Turing, A. M. The chemical basis of morphogenesis. *Bull. Math. Biol.* **52**, 153–197 (1990).
24. DeGiorgio, V. & Scully, M. O. Analogy between the laser threshold region and a second-order phase transition. *Phys. Rev. A* **2**, 1170 (1970).
25. Wright, L. G., Christodoulides, D. N. & Wise, F. W. Spatiotemporal mode-locking in multimode fiber lasers. *Science* **358**, 94–97 (2017).
26. Gordon, A. & Fischer, B. Phase transition theory of many-mode ordering and pulse formation in lasers. *Phys. Rev. Lett.* **89**, 103901 (2002).
27. Stanley, H. E. *Phase Transitions and Critical Phenomena*. (Clarendon Press, 1971).
28. Prigogine, I. & Lefever, R. Symmetry breaking instabilities in dissipative systems. II. *J. Chem. Phys.* **48**, 1695–1700 (1968).
29. Wilczek, F. Quantum time crystals. *Phys. Rev. Lett.* **109**, 160401 (2012).
30. Else, D. V., Bauer, B. & Nayak, C. Floquet time crystals. *Phys. Rev. Lett.* **117**, 090402 (2016).
31. Dechoum, K., Rosales-Zárate, L. & Drummond, P. D. Critical fluctuations in an optical parametric oscillator: when light behaves like magnetism. *J. Opt. Soc. Am. B* **33**, 871–883 (2016).
32. Drummond, P. D., McNeil, K. J. & Walls, D. F. Non-equilibrium transitions in sub/second harmonic generation. *Opt. Acta* **27**, 321–335 (1980).
33. Kuznetsov, A. V. Optical bistability driven by a first order phase transition. *Opt. Commun.* **81**, 106–111 (1991).
34. Gol'Tsman, G. N. et al. Picosecond superconducting single-photon optical detector. *Appl. Phys. Lett.* **79**, 705–707 (2001).
35. Yang, L.-P. & Jacob, Z. Quantum critical detector: amplifying weak signals using discontinuous quantum phase transitions. *Opt. Express* **27**, 10482–10494 (2019).
36. Di Candia, R., Minganti, F., Petrovnin, K. V., Paraoanu, G. S. & Felicetti, S. Critical parametric quantum sensing. Preprint at https://doi.org/2107.04503 (2021).
37. Del Bino, L., Silver, J. M., Stebbings, S. L. & Del'Haye, P. Symmetry breaking of counter-propagating light in a nonlinear resonator. *Sci. Rep.* **7**, 43142 (2017).
38. Wang, C. et al. A nonlinear microresonator refractive index sensor. *J. Lightwave Technol.* **33**, 4360–4366 (2015).
39. Kaplan, A. E. & Meystre, P. Enhancement of the Sagnac effect due to nonlinearly induced nonreciprocity. *Opt. Lett.* **6**, 590–592 (1981).
40. Wang, C. et al. Nonlinearly enhanced refractive index sensing in coupled optical microresonators. *Opt. Lett.* **39**, 26–29 (2014).
41. Hamerly, R. et al. Reduced models and design principles for half-harmonic generation in synchronously pumped optical parametric oscillators. *Phys. Rev. A* **94**, 063809 (2016).
42. Hodaei, H. et al. Enhanced sensitivity at higher-order exceptional points. *Nature* **548**, 187–191 (2017).
43. Leefmans, C. et al. Topological dissipation in a time-multiplexed photonic resonator network. *Nat. Phys.* **18**, 442–449 (2022).
44. Ding, J., Belykh, I., Marandi, A. & Miri, M.-A. Dispersive versus dissipative coupling for frequency synchronization in lasers. *Phys. Rev. Appl.* **12**, 054039 (2019).
45. Lee, K. F. et al. Carrier envelope offset frequency of a doubly resonant, nondegenerate, mid-infrared gaas optical parametric oscillator. *Opt. Lett.* **38**, 1191–1193 (2013).
46. Krioukov, E., Klunder, D. J. W., Driessen, A., Greve, J. & Otto, C. Sensor based on an integrated optical microcavity. *Opt. Lett.* **27**, 512–514 (2002).
47. Heideman, R. G. & Lambeck, P. V. Remote opto-chemical sensing with extreme sensitivity: design, fabrication and performance of a pigtailed integrated optical phase-modulated mach–zehnder interferometer system. *Sens. Actuators B: Chem.* **61**, 100–127 (1999).
48. Ren, J. et al. Ultrasensitive micro-scale parity-time-symmetric ring laser gyroscope. *Opt. Lett.* **42**, 1556–1559 (2017).
49. Puckett, M. W. et al. 422 Million intrinsic quality factor planar integrated all-waveguide resonator with sub-mhz linewidth. *Nat. Commun.* **12**, 934 (2021).
50. Jankowski, M. et al. Ultrabroadband nonlinear optics in nanophotonic periodically poled lithium niobate waveguides. *Optica* **7**, 40–46 (2020).
51. Lu, J. et al. Ultralow-threshold thin-film lithium niobate optical parametric oscillator. *Optica* **8**, 539–544 (2021).
52. Guo, Q. et al. Femtojoule femtosecond all-optical switching in lithium niobate nanophotonics. *Nat. Photonics* **16**, 625–631 (2022).
53. Tusnin, A. K., Tikan, A. M., Komagata, K. & Kippenberg, T. J. Coherent dissipative structures in chains of coupled $\chi^{(3)}$ resonators. Preprint at https://arxiv.org/abs/2104.11731 (2021).
54. Longhi, S. & Geraci, A. Swift-hohenberg equation for optical parametric oscillators. *Phys. Rev. A* **54**, 4581 (1996).
55. Okawachi, Y. et al. Dual-pumped degenerate kerr oscillator in a silicon nitride microresonator. *Opt. Lett.* **40**, 5267–5270 (2015).
56. Wu, L.-A., Kimble, H. J., Hall, J. L. & Wu, H. Generation of squeezed states by parametric down conversion. *Phys. Rev. Lett.* **57**, 2520 (1986).
57. Gatti, A. & Lugiato, L. Quantum images and critical fluctuations in the optical parametric oscillator below threshold. *Phys. Rev. A* **52**, 1675 (1995).
58. Longhi, S. Nonadiabatic pattern formation in optical parametric oscillators. *Phys. Rev. Lett.* **84**, 5756 (2000).
59. Menotti, M. et al. Nonlinear coupling of linearly uncoupled resonators. *Phys. Rev. Lett.* **122**, 013904 (2019).

Methods

Experimental setup

The simplified experimental schematic is shown in Fig 1e, a detailed version of which is presented as Supplementary Fig 1 (Supplemental Section 1). The OPO pump is derived from a mode-locked laser (1,550 nm at 250 MHz) through second-harmonic generation in a bulk periodically poled lithium niobate (PPLN) crystal. The main cavity repetition rate is a quarter of the repetition rate of the mode-locked laser and is composed of a PPLN waveguide (a reverse proton exchange waveguide that phase matches the interaction between pump photons at 775 nm and signal and/or idler photons around 1,550 nm)[60,49] with fibre-coupled output ports, a piezo-mounted translation stage (to provide the cavity detuning), a free-space section (to match the pump repetition rate to be a multiple of the free spectral range of the cavity), an additional fiber segment to engineer the cavity dispersion (dispersion compensating fibers) and a couple of beam splitters (which provide the output coupling and interface with the coupling cavity). The coupling cavity repetition rate is half the repetition rate of the mode-locked laser and comprises several gold mirrors and a piezotranslation stage (to adjust the coupling phase). Additional details pertaining to the experimental setup and methods are provided in the Supplementary Information (Supplemental Section 1).

System modelling

The parametric nonlinear interaction in the PPLN waveguide (length L) is governed by:

$$\frac{\partial a}{\partial z} = \left[-\frac{\alpha^{(a)}}{2} - \mathrm{i}\frac{\beta_2^{(a)}}{2!}\frac{\partial^2}{\partial t^2} + \ldots\right]a + \epsilon a^* b \tag{1}$$

$$\frac{\partial b}{\partial z} = \left[-\frac{\alpha^{(b)}}{2} - u\frac{\partial}{\partial t} - \mathrm{i}\frac{\beta_2^{(b)}}{2!}\frac{\partial^2}{\partial t^2} + \ldots\right]b - \frac{\epsilon a^2}{2} \tag{2}$$

The evolution of the signal (a) and the pump (b) envelopes in the slowly varying envelope approximation are dictated by equations (1a) and (1b), respectively[41]. Here u represents the walk-off parameter, α denotes the attenuation coefficients and the GVD coefficients are denoted by β. The effective second-order nonlinear coefficient (ε) is related to the second-harmonic generation efficiency[41]. Additionally, the OPO fields experience the effect of the coupling and the cavity feedback every round trip:

$$a_1' = \sqrt{1-|\kappa|^2}a_1 + |\kappa|\mathrm{e}^{\mathrm{i}\theta}a_2 \tag{3}$$

$$a_2' = \sqrt{1-|\kappa|^2}a_2 + |\kappa|\mathrm{e}^{\mathrm{i}\theta}a_1 \tag{4}$$

where the subscripts 1 and 2 refer to the OPO1 and the OPO2, respectively, comprising the coupled OPO. The coupling strength is denoted by $|\kappa|$, and θ is the coupling phase:

$$a_{(1,2)}^{(n+1)}(0,t) = \mathcal{F}^{-1}\left\{G_0^{-\frac{1}{2}}\mathrm{e}^{\mathrm{i}\bar{\phi}}\mathcal{F}\left\{a_{(1,2)}'^{(n)}(L,t)\right\}\right\} \tag{5}$$

$$\bar{\phi} = \Delta\phi + \frac{l\lambda^{(a)}}{2c}(\delta\omega) + \frac{\phi_2}{2!}(\delta\omega)^2 + \ldots \tag{6}$$

Equations (5 and 6) includes the round-trip loss, which is lumped into an aggregated out-coupling loss factor G_0, the GVD (ϕ_2) of the cavity and the detuning ($\Delta\phi$) ($\Delta\phi = \pi l$, where l is the cavity length detuning in units of signal half-wavelengths) of the circulating signal from the exact synchrony. The round-trip number is denoted by n. $\mathcal{F}$ denotes the Fourier transform operation. The equations are numerically solved adopting the split-step Fourier algorithm.

Data availability

Source data are available for this paper and can be found at https://doi.org/10.6084/m9.figshare.21252147. All other data that support the plots within this paper and other findings of this study are available from the corresponding author upon reasonable request.

Code availability

The codes that support the findings of this study are available from the corresponding author upon reasonable request.

References

60. Langrock, C. & Fejer, M. M. Fiber-feedback continuous-wave and synchronously-pumped singly-resonant ring optical parametric oscillators using reverse-proton-exchanged periodically-poled lithium niobate waveguides. *Opt. Lett.* **32**, 2263–2265 (2007).

Acknowledgements

We thank S. Jahani and M. Gyun Suh for helpful discussions. We acknowledge support from ARO grant no. W911NF-18-1-0285 (A.M.), AFOSR award FA9550-20-1-0040 (A.M.), NSF grant nos. 1846273 (A.M.) and 1918549 (A.M.), and NASA. We wish to thank NTT Research for their financial and technical support.

Author contributions

A.R. and A.M. conceived the idea. A.R. performed the experiments with help from R.N. A.R. developed the theory and performed the numerical simulations. C.L. fabricated the PPLN waveguide used in the experiment with the supervision of M.F. A.R. and A.M. wrote the manuscript with input from all authors. A.M. supervised the project.

Competing interests

The authors declare no competing interests.

Additional information

Supplementary information The online version contains supplementary material available at https://doi.org/10.1038/s41567-022-01874-8.

Correspondence and requests for materials should be addressed to Alireza Marandi.

Peer review information *Nature Physics* thanks the anonymous reviewers for their contribution to the peer review of this work.